

## Photostability versus Photodegradation in the Excited-State Intramolecular Proton Transfer of Nitro Enamines: Competing Reaction Paths and Conical Intersections

Anna Paola Migani,<sup>\*,†</sup> Michael J. Bearpark,<sup>‡</sup> Massimo Olivucci,<sup>§,⊥</sup> and Michael A. Robb<sup>\*,‡</sup>

Contribution from the Institut de Química Computacional, Departament de Química, Universitat de Girona, Campus de Montilivi, 17071 Girona, Spain, Department of Chemistry, Imperial College London, South Kensington Campus, London SW7 2AZ, UK, Dipartimento di Chimica, Università di Siena, 53100 Siena, Italy, and Centro per lo Studio dei Sistemi Complessi, Università di Siena, via Pendola 37, Siena, Italy

Received September 12, 2006; E-mail: amigani@stark.udg.es; mike.robb@imperial.ac.uk

**Abstract:** The phototautomerization mechanism of a model nitro enamine (NEA) chromophore (incorporated in the structure of a highly photolabile pesticide, tetrahydro-2-(nitromethylene)-2H-1,3-thiazine) has been studied using complete active space self-consistent field reaction path computations. The optically accessible  ${}^1\pi\pi^*$  excited state of NEA involves separation of charge and correlates diabatically with the ground state of the tautomerized acinitro imine (ANI) form. For optimum photostabilization, the  ${}^1\pi\pi^*$  state of NEA should be  $S_1$ : in this case, the tautomer would be efficiently formed via a diabatic intramolecular proton-transfer pathway passing through an  $S_1/S_0$  conical intersection, followed by a facile thermal back proton-transfer reaction. However, in NEA itself the lowest excited states correspond to nitro group  ${}^1n\pi^*$  states, and there are additional surface crossings that provide a mechanism for populating the  ${}^1n\pi^*$  manifold. The above results indicate that the high photolability observed for the pesticide [Kleier, D.; Holden, I.; Casida, J. E.; Ruzo, L. O. *J. Agric. Food Chem.* 1985, 33, 998–1000] has to be ascribed to photochemistry originating on the  ${}^1n\pi^*$  manifold of states, populated indirectly from the  ${}^1\pi\pi^*$  state.

### 1. Introduction

Understanding the molecular mechanism of photostabilization is of importance for the protection of chemical systems from photodegradation. Recent theoretical work has suggested several photochemical deactivation mechanisms from  ${}^1n\pi^*$ ,<sup>1–6</sup>  ${}^1\pi\pi^*$ ,<sup>7,8</sup> and  ${}^1\pi\sigma^*$ <sup>9–11</sup> states. In all cases deactivation involve a conical intersection (CI)<sup>11</sup> funnel lying along a bond rupture coordinate. For photostability, deactivation at conical intersection does not

lead to chemical change via product formation but rather leads to (a) the direct photophysical regeneration of the original ground-state ( $S_0$ ) structure or (b) the production of a short-lived ground-state intermediate that efficiently reverts to the original  $S_0$  structure through a thermal reaction. The present study is directed at the excited-state deactivation mechanism of a nitro enamine model system (**1** in Scheme 1) based on a phototautomerization process (nitro enamine (NEA)/acinitro imine (ANI) phototautomerization in Scheme 1).

Nitro enamines are incorporated in the chemical structure of several molecules with biological activity exploited in agriculture,<sup>12,13</sup> among them the remarkably potent insecticide tetrahydro-2-(nitromethylene)-2H-1,3-thiazine<sup>14</sup> (**2** in Scheme 1). In these systems, the nitro enamine portion provides a channel for the photostabilization by benign dissipation of the light energy through the phototautomerization process shown in Scheme 1. However, structure **2** is, in practice, not photostable and degrades upon sunlight<sup>12</sup> exposure and direct irradiation<sup>14</sup> with lifetimes

<sup>†</sup> Institut de Química Computacional.

<sup>‡</sup> Imperial College London.

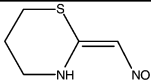
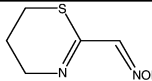
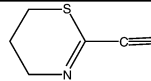
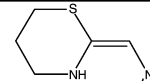
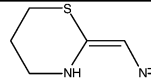
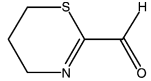
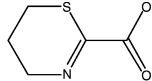
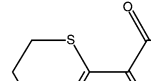
<sup>§</sup> Dipartimento di Chimica, Università di Siena.

<sup>⊥</sup> Centro per lo Studio dei Sistemi Complessi, Università di Siena.

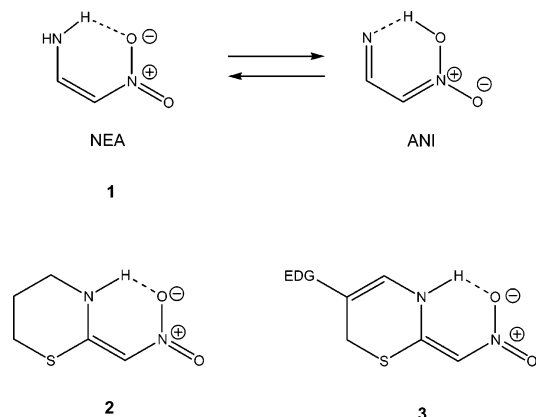
- (1) Ismail, N.; Blancafort, L.; Olivucci, M.; Kohler, B.; Robb, M. A. *J. Am. Chem. Soc.* **2002**, *124*, 6818–6819.
- (2) Nau, W. M.; Greiner, G.; Wall, J.; Rau, H.; Olivucci, M.; Robb, M. A. *Angew. Chem., Int. Ed.* **1998**, *37*, 98–101.
- (3) Paterson, M. J.; Robb, M. A.; Blancafort, L.; DeBellis, A. D. *J. Am. Chem. Soc.* **2004**, *126*, 2912–2922.
- (4) Sinicropi, A.; Pischel, U.; Basosi, R.; Nau, W. M.; Olivucci, M. *Angew. Chem., Int. Ed.* **2000**, *39*, 4582–4586.
- (5) Sinicropi, A.; Pogni, R.; Basosi, R.; Robb, M. A.; Gramlich, G.; Nau, W. M.; Olivucci, M. *Angew. Chem., Int. Ed.* **2001**, *40*, 4185–4189.
- (6) Estevez, C. M.; Bach, R. D.; Hass, K. C.; Schneider, W. F. *J. Am. Chem. Soc.* **1997**, *119*, 5445–5446.
- (7) Blancafort, L.; Gonzales, D.; Olivucci, M.; Robb, M. A. *J. Am. Chem. Soc.* **2002**, *124*, 6398–6406.
- (8) Merchan, M.; Serrano-Andrés, L. *J. Am. Chem. Soc.* **2003**, *125*, 8108–8109.
- (9) Sobolewski, A. J.; Domcke, W. *J. Phys. Chem. A* **1999**, *103*, 4494–4504.
- (10) Sobolewski, A. L.; Domcke, W.; Dedonder-Lardeux, C.; Jouvet, C. *Phys. Chem. Chem. Phys.* **2002**, *4*, 1093–1100.
- (11) Bernardi, F.; Olivucci, M.; Robb, M. A. *Chem. Soc. Rev.* **1996**, 321–328.

- (12) Kleier, D. A. In *Comparing Glasshouse and Field Pesticide Performance II*; Hewitt, H. G.; Caseley, J.; Copping, L. G.; Grayson, B. T.; Tyson, D., Eds.; Farnham: Surrey, U.K., 1994; Vol. 59, p 97.
- (13) Solway, S. B.; Henry, A. C.; Kollmeyer, W. D.; Padgett, W. M.; Powell, J. E.; Roman, S. A.; Tieman, C. H.; Corey, R. A.; Horne, C. A. In *Pesticides and Venom Neurotoxicity*; Shankland, D. L., Hollingworth, R. M., Smyth, T. J., Eds.; Plenum Publishing: New York, 1978; p 153.
- (14) Kleier, D.; Holden, I.; Casida, J. E.; Ruzo, L. O. *J. Agric. Food Chem.* **1985**, *33*, 998–1000.

**Table 1.** Photoproducts Resulting from Irradiation of **2**; Yields at 30% of Conversion (adapted from ref 14)

Reduced Species				
				
1	2	3	4	5
<5% <sup>1</sup>	<5% <sup>1</sup>	22% <sup>1</sup>	<5% <sup>1</sup>	~10% <sup>1</sup>
<5% <sup>2</sup>	<5% <sup>2</sup>	<5% <sup>2</sup>	<5% <sup>2</sup>	15-20% <sup>2</sup>
Oxidized Species				
				
6	7	8		
--	--	--		
<1% <sup>2</sup>	<1% <sup>2</sup>	<1% <sup>2</sup>		

<sup>1</sup> CH<sub>2</sub>Cl<sub>2</sub> solvent. <sup>2</sup> H<sub>2</sub>O or CH<sub>3</sub>OH solvent.

**Scheme 1**

ranging from 10 min in water to 1 min in dichloromethane.<sup>13</sup> The photoproducts and corresponding yields obtained in both types of solvents upon direct irradiation<sup>14</sup> are shown in Table 1.

The intense band ( $\epsilon \approx 40,000$ ) in the absorption spectrum ( $\lambda = 365$  nm in water and in methanol) of **2** corresponds to a  $^1\pi\pi^*$  state with partial charge separation character between the enamine and the nitro functionality.<sup>14</sup> Thus, the phototautomerization in the pesticide is initiated upon excitation to the  $^1\pi\pi^*$  state, followed by excited-state intramolecular proton transfer (ESIPT) from the amine to the nitro group, to generate the ground-state tautomerized form corresponding to an ANI derivative.<sup>14</sup> Obviously, photostability would be the result if the tautomerized form reverted to the starting tautomer (mechanism **b** discussed above), and this in turn would occur if the barrier associated with this path were very low and other possible pathways on the ground-state surface leading to different products could not compete.

Photolysis experiments carried out in deuterated protic solvents have shown that the pesticide ANI derivative is formed only photochemically, and once formed it promptly reverts to the original tautomer through a thermal back proton-transfer mechanism catalyzed by protic solvents.<sup>14</sup> Thus, there is experimental proof that (at least in protic solvents) the phototautomerization occurs as a cyclic pathway, which returns the pesticide back to its ground-state untautomerized form without net reaction. Nevertheless, even in protic solvents, upon prolonged irradiation, degradation products accumulate in the photolysate.<sup>14</sup> This points to the existence of a “leak” in the photocycle, which is responsible for the deactivation of the pesticide via other photochemical processes that ultimately lead to degradation products. In the present work we identify possible sources of inefficiency in the photocycle associated with the IPT coordinate and discern the mechanism of degradation of **2**.

Because the mechanistic ideas are rather complex, we have chosen to organize this paper in a slightly unconventional way. Thus, in the following section (section 2) we discuss all the central features of the network of pathways associated with the phototautomerization coordinate of model **1**. The mechanistic features are unified and rationalized with the use of simple VB structures. Then, after a digression to discuss the computational details in section 3, we present all the computations (sections 4 and 5) that support the global mechanistic scenario discussed in section 2. Finally, in section 6 we discuss the photodegradation of pesticide **2** and how the photostability of systems such as **2** could be improved.

**2. Mechanistic Overview**

We begin with a discussion of the possible states involved in the NEA/ANI phototautomerization. In model **1**, the optical excitation is to the  $^1\pi\pi^*$  state. However, this is not the lowest-energy excited state. The lowest-energy states are quasi-

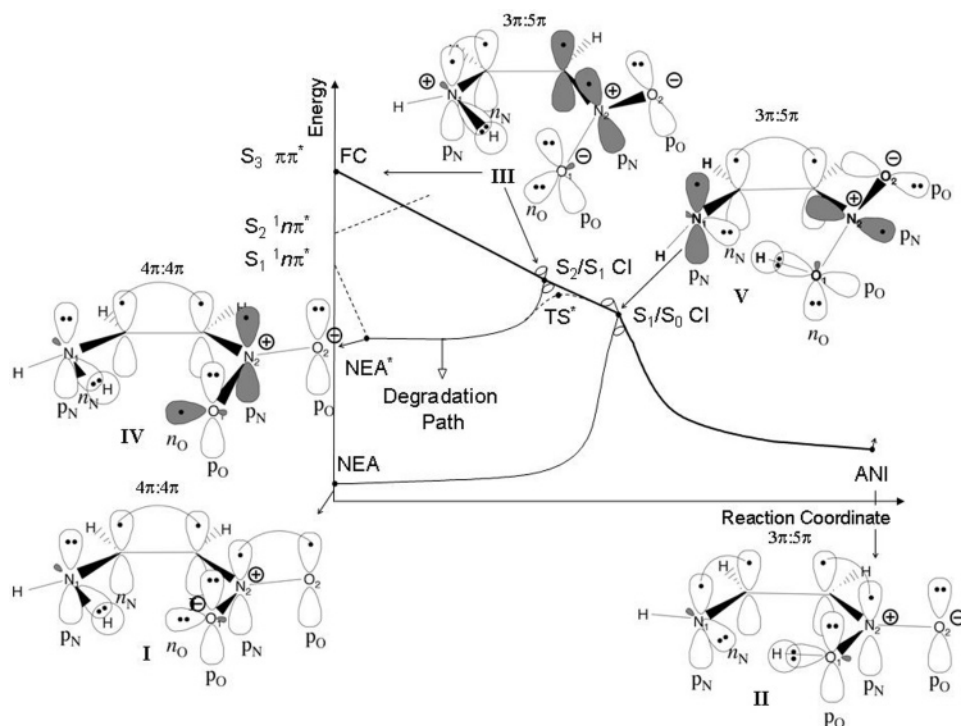


**Figure 1.** Nitro enamine (NEA)/acinitro imine (ANI) intramolecular excited-state proton-transfer reaction for **1** (Scheme 1): the bold line follows the optically excited  $^1\pi\pi^*$  state, which crosses the NEA  $^1n\pi^*$  excited-states from top left to bottom right where it becomes the ground state. The  $\pi$ -electron arrangement is denoted by using the  $n\pi:m\pi$  notation indicating the number of  $\pi$ -electrons associated with the nitro(acinitro)-enamine(azoallyl) fragments.

degenerate nitro group  $^1n\pi^*$  states where the  $n$  orbitals are the plus/minus combination of the oxygen lone pairs,  $n_s$  and  $n_a$ , respectively. Note that the  $^1n_a\pi^*$  has the tendency to localize at relaxed geometries on the  $O_{(1)}$  oxygen, so that it can also be described as involving excitation from the  $O_{(1)}$   $n$  orbital.

The relative energetic behavior of the  $^1\pi\pi^*$  and  $^1n\pi^*$  potential energy surfaces along the phototautomerization reaction coordinate controls the photostability of the pesticide. The results from the present work are illustrated schematically in Figure 1 along with a valence bond (VB) representation of these states.

From Figure 1, one can see that, on the ground state, the two tautomers are interconvertible by means of intramolecular hydrogen migration, which occurs in the form of a coupled “in-plane” proton shift and “out-of-plane” electron migration (see VB structures **I** and **II**). In order to understand this, it is convenient to divide the NEA and ANI tautomers in two subunits, enamine/nitro and azoallyl/acinitro, respectively. The electron-transfer process is represented by an interchange of positions of single and double bonds, and involves the eight  $\pi$ -electron system. The enamine and nitro fragments have four  $\pi$ -electrons each, whereas the azoallyl and acinitro groups carry three and five  $\pi$ -electrons, respectively. The proton transfer involves a four-electron/two-orbital system corresponding to the  $N_{(1)}-H$   $\sigma$  orbital and the oxygen ( $O_{(1)}$ ) lone pair in the NEA structure, and the  $O_{(1)}-H$   $\sigma$  orbital and the nitrogen ( $N_{(1)}$ ) lone pair in the ANI structure.

The NEA and ANI tautomers can also be interconverted photochemically, and clearly the photochemical process must also involve the transfer of an electron and proton from one end of the molecule to the other. The electron transfer is accomplished by electronic excitation to the  $^1\pi\pi^*$  state (VB structure **III**). (Note that, although the  $^1\pi\pi^*$  state has only partial charge separation character at the FC point, in the VB

description of this state we assume the electron transfer to be complete. This helps to visualize the diabatic correlation between the  $^1\pi\pi^*$  state at FC and the ANI tautomer on  $S_0$ .) The enamine and nitro fragments then become positively and negatively charged, with three and five  $\pi$ -electrons respectively. There is an analogous  $\pi$ -electron arrangement in the ground-state ANI tautomer (VB structure **II**), with three and five  $\pi$ -electrons associated with the azoallyl and acinitro units, respectively, which indicates that the two structures correlate diabatically and are connected through the transfer of a proton, which is released by the positively charged enamine fragment and is picked up by the negatively charged nitro fragment. Since the excited-state reactant and the ground-state product lie on the same diabatic surface, the process could be even classified as an “adiabatic” reaction by following a classification scheme proposed by Turro.<sup>15</sup>

Figure 1 shows that the  $^1\pi\pi^*$  state corresponds to  $S_3$  in system **1** and that there is a sequence of three crossings that convert the  $^1\pi\pi^*$  state from  $S_3$  at the NEA tautomer into the ground state at the ANI tautomer. The first two crossings occur between the  $^1\pi\pi^*$  state and the  $^1n\pi^*$  states. In particular the second crossing involves the  $^1n\pi^*$  state, where the oxygen that carries the half-filled  $n$  orbital,  $O_{(1)}$ , faces the amine group (VB structure **IV**), and corresponds to a conical intersection ( $S_2/S_1$  CI). The third crossing also corresponds to a conical intersection ( $S_1/S_0$  CI) and occurs between the  $^1\pi\pi^*$  state and the ground state. Thus, the diabatic correlation and the relative order of  $^1\pi\pi^*$  and  $^1n\pi^*$  states implies that the NEA/ANI phototautomerization proceeds entirely on the  $^1\pi\pi^*$  energy surface via a sequence of three surface crossings. It follows from this that the reaction coordinate leads directly to the surface crossings, going through

(15) Turro, N. J.; McVey, J.; Ramamurthy, V.; Lechtken, P. *Angew. Chem., Int. Ed.* **1979**, *18*, 572–586.

each of them. This means—with respect to the  $S_2/S_1$  and  $S_1/S_0$  conical intersections—that the reaction coordinate must lie in the branching space defined by the gradient difference ( $\mathbf{x}_1$ ) and derivative coupling ( $\mathbf{x}_2$ ) vectors that lift the degeneracy between the states at first order at the  $S_2/S_1$  and  $S_1/S_0$  conical intersections. Thus, whether we are considering the  $S_1/S_0$  conical intersection or the  $S_2/S_1$  conical intersection, the branching space coordinates will involve the proton-transfer motion, in addition to the other nuclear modes that describe the reaction coordinate such as bond alternation along the backbone and, as discussed below, an out-of-plane mode.

The fact that the excited-state reaction coordinate is barrierless is consistent with the fact that the IPT corresponds to a charge recombination process (see discussion above relative to structures **II** and **III**), and leads to a stabilization of the  $^1\pi\pi^*$  state with charge-separation character.<sup>16</sup> Accordingly, the reaction rate will be in the femtosecond range. This explains that the formation of the ANI derivative of pesticide **2** is observed in the photolysate before the formation of degradation products.<sup>14</sup>

The IPT is found to be essentially complete at the  $S_1/S_0$  CI, as shown by structure **V**, which is the same as structure **III** but with the proton migrated to the nitro side and coupled with the  $O_{(1)}$   $p_\pi$ -orbital electrons, and a different coupling of the  $N_{(1)}$ -CCN<sub>(2)</sub>  $\pi$ -electrons. Comparison of structures **III** and **V** also shows that the mechanism of phototautomerization on the  $^1\pi\pi^*$  state corresponds to proton abstraction from the  $N_{(1)}$ -H  $\sigma$  orbital carried out by the nitro group  $\pi$ -electron system ( $O_{(1)}$   $p_\pi$ -orbital). It follows that the reaction is a pericyclic reaction, where the net result is the conversion of one  $\pi$ -bond into a  $\sigma$ -bond. Since the proton is transferred from position 1 to position 5 within the  $\pi$ -electron system, the reaction can be classified as [1,5]-sigmatropic H-shift.<sup>17</sup> Another important point that is evident from the comparison of VB structures **III** and **V** is that the nitro group, in order to be able to abstract the proton, must move out of the average molecular plane. Hence, another important component of the geometrical deformation along the reaction coordinate, and of the branching planes (in addition to the proton transfer and skeletal stretching), will be provided by out-of-plane motion.

There is one additional point that arises from the consideration of VB structures in Figure 1 and results in a characteristic  $S_1/S_0$  conical intersection. If we consider the VB structures **III** and **I** that conically intersect at the  $S_1/S_0$  crossing, it is clear that the VB structure **III** corresponds to a dot–dot configuration, whereas the VB structure **I** corresponds to hole–pair configuration, so that the  $S_1/S_0$  conical intersection is of the type dot–dot/hole–pair.<sup>18,19</sup> Moreover, the  $S_1/S_0$  conical intersection features twisting about the bond connecting the donor and acceptor moieties that interchange the electron and the proton (the double bond  $C=N_{(2)}O_2H$  of the ANI derivative in Scheme 1). Dot–dot/hole–pair  $S_1/S_0$  intersections with a twisted geometry about the donor/acceptor bond might be a general phenomenon in ESIPT. To this respect it is interesting to note that

another example of intramolecular proton migration mediated by a twisted dot–dot/hole–pair type funnel is found in ethylene.<sup>20,21</sup> Conical intersection points can be identified in the seam of intersections mediating the  $Z/E$  photoisomerization that also have some H-migration character between the two twisted methylene moieties. Similarly to **1**, their branching planes have significant H-migration character (in addition to twisting and pyramidalization modes) and can mediate [1,2]-sigmatropic H-shift to form ethylidene.<sup>20,21</sup>

Ground-state relaxation to the ANI tautomer at the  $S_1/S_0$  CI has a higher probability, based on the consideration that this path is the “direct” continuation of the excited-state coordinate that does not involve a change of electronic configuration upon radiationless decay, and that the proton transfer is found to be essentially complete at the  $S_1/S_0$  CI. Despite this, in Figure 1 the position of the crossing has been represented as intermediate between that of the two ground-state tautomers. This is because, as discussed above, the reaction coordinate is multimodal. Thus, although from the point of view of the proton transfer the  $S_1/S_0$  CI can be classified as an ANI-like structure, from the point of view of the skeletal bond lengths it resembles the NEA ground-state structure and similarly features a single/double/single  $N_{(1)}$ -CCN<sub>(2)</sub> bond pattern. Thus, formation of the ground-state ANI intermediate simply involves a  $N_{(1)}$ -CCN<sub>(2)</sub> skeletal rearrangement coupled with return to planarity, and no motion of the proton. The computed barrier for back proton transfer (ANI→NEA path) on the ground state is  $\sim 1$  kcal mol<sup>-1</sup>, allowing for efficient regeneration of NEA from ANI.

So far we have seen that the formation of the ANI intermediate following decay at the  $S_1/S_0$  CI is predicted to be very efficient. However, we have also seen that the system must go through additional surface crossings before reaching the  $S_1/S_0$  CI. The presence of these crossings has a detrimental effect on the photostability of system **1**, since they represent “leakage” points in the phototautomerization cycle. The discussion will be made with reference to the  $S_2/S_1$  CI since we are concerned with the population of  $S_1$  starting from  $S_2$ . At this crossing point the molecule may continue its journey on the  $^1\pi\pi^*$  excited-state toward the low-lying  $S_1/S_0$  CI or may be diverted onto the  $^1n\pi^*$  state, i.e., branching of the reaction coordinate. Decay to the  $^1n\pi^*$  state at the  $S_2/S_1$  CI has some probability although it implies a change of electronic state due to the crossing topography: as shown in Figure 1 (see also Figure S1), the computed  $S_1$   $^1n\pi^*$  relaxation path is steeper than the  $S_1$   $^1\pi\pi^*$  one. Moreover, the length of the derivative coupling is large compared to the gradient difference (0.1 versus 0.06 au), supporting the fact that the excited molecule has some probability to change electronic state at the crossing. The leakage might be “small”, but over many phototautomerization cycles it would cause the complete degradation of the molecule.

Obviously, one possible decay route from the  $S_1$   $^1n\pi^*$  state is represented by the  $S_1/S_0$  CI. However, Figure 1 shows that the  $S_1$   $^1n\pi^*$  state is separated from the  $S_1/S_0$  CI by a sizable energy barrier that can be rationalized by an avoided crossing with the  $^1\pi\pi^*$  state. This implies that from the  $S_1$   $^1n\pi^*$  state the excited molecule will follow competing low-energy pho-

(16) Michl, J.; Bonacic-Koutecky, V. *Electronic Aspects of Organic Photochemistry*; Wiley: New York, 1990.

(17) Turro, N. J. *Modern Molecular Photochemistry*, The Benjamin/Cummings Publishing Co. Inc.: Menlo Park, 1978.

(18) Bonacic-Koutecky, V.; Koutecky, J.; Michl, J. *Angew. Chem., Int. Ed. Engl.* **1987**, *26*, 170–189.

(19) Migani, A.; Olivucci, M. Conical Intersections and Organic Reaction Mechanisms. In *Conical Intersections: Electronic Structure, Dynamics, and Spectroscopy*; Domeke, W., Yarkony, D. R., Köppel, H., Eds.; World Scientific: River Edge, NY, 2004; pp 271–320.

(20) Ben-Nun, M.; Martinez, T. J. *Chem. Phys. Lett.* **1998**, *298*, 57–65.

(21) Ben-Nun, M.; Martinez, T. J. *Chem. Phys.* **2000**, *259*, 237–248.

tochemical routes typical of the nitro group  ${}^1n\pi^*$  state<sup>22</sup> that ultimately leads to irreversible photoproducts (i.e., degradation).

### 3. Computational Details

In this work, the mapping of the phototautomerization coordinate (Figure 1) for model chromophore **1** (Scheme 1) is carried out by constructing the photochemical reaction path.<sup>23</sup> This is defined as the minimum energy path (MEP) computed in mass-weighted Cartesian coordinates that connects the Franck–Condon (FC) region of the excited-state potential energy surface to the possible radiationless deactivation channels, in the full space of the  $3N - 6$  vibrational degrees of freedom of the molecule (where  $N$  is the number of atoms).

For these computations, we have employed the complete active space self-consistent field (CASSCF) method, with appropriate active spaces and the 6-31G\* basis set. The initial relaxation directions (IRDs) were computed as described in ref 24. The conical intersection funnels are rigorously determined by using state-averaged orbitals and the optimization procedure<sup>25</sup> available in the Gaussian series of programs.<sup>26</sup>

The choice of active space in our computations requires some comment. The full active space comprises the  $\sigma/\sigma^*$  orbitals of the  $N_{(1)}-H$  bond, the symmetric and antisymmetric combination of the two oxygen n orbitals (i.e.,  $n_s$  and  $n_a$  respectively), the  $\pi/\pi_{nb}/\pi^*$  orbitals of the nitro group (i.e., bonding, nonbonding, and antibonding respectively), the  $\pi/\pi^*$  orbitals of the C=C double bond, and the lone pair orbital of the amine group, giving a total of 14 active electrons in 10 active orbitals (14e/10o). This active space provide a balanced description of the lowest four singlet states ( $S_0$ ,  ${}^1n_s\pi^*$ ,  ${}^1n_a\pi^*$ ,  ${}^1\pi\pi^*$ ) of **1** along the ES IPT coordinate.

We have nevertheless used different active spaces for different regions of the potential energy surface as a consequence of eliminating redundant orbitals (those with occupations close to 2.0 or 0.0) from the full active space, to avoid convergence problems. To compute the  $S_1$  relaxation paths starting at the  $S_2/S_1$  CI (Figure S1), and the  $NEA^* \rightarrow TS^* \rightarrow S_1/S_0$  CI phototautomerization coordinate (Figure S2) a 12e/10o active space—without the doubly occupied n orbital centered on the oxygen atom labeled ( $O_{(2)}$ )—was used. However, in the region of the  $S_1/S_0$  crossing, the n orbital of the abstracting oxygen ( $O_{(1)}$ ) also becomes redundant. Thus, the location of the lowest-energy point in the intersection space and computation of the associated ground-state relaxation paths (Figure S3) were carried out using a reduced 10e/8o active space. The  $S_0$  NEA,  $S_0$  ANI, and ground-state TS geometries were optimized using smaller 6e/5o active spaces. The 6e/5o active space used for the optimization of the  $S_0$  NEA structure involves the  $\pi/\pi_{nb}/\pi^*$  orbitals of the nitro group and  $\pi/\pi^*$  orbitals of the C=C double bond, whereas the 6e/5o active space used for the optimization of the  $S_0$  ANI and  $S_0$  TS is different, comprising the  $\pi/\pi^*$  orbitals of the  $N_{(1)}=C$  and  $C=N_{(2)}$  double bonds, and the  $O_{(2)}$   $p_\pi$  orbital.

The general approach taken in this work has been to optimize the critical points using the minimum orbital active space required, subsequently enlarging the active space only to make connections between critical points or to compare energies. (However, direct comparison of energies is only possible when the same active space has been used. See discussion and Figure S4 in the Supporting Information regarding the validity of the adopted computational strategy.) Thus, the  $S_2/S_1$  CI optimization requires a 12e/9o active space,

whereas the  $S_1/S_0$  CI, a 10e/8o active space, which is, as discussed above, a subspace of the 12e/9o active space. Accordingly, the 12e/9o active space was used to compute the MEP connecting the two points. Similarly, the 6e/5o active spaces used to optimize the  $S_0$  NEA and ACI tautomers are subspaces of the 10e/8o active space used to locate  $S_1/S_0$  CI. Accordingly, the 10e/8o active space was used to compute the ground-state relaxation paths originating at  $S_1/S_0$  CI, since it contains all the configurations relevant to describe accurately the  $S_1/S_0$  CI region, as well as those that are important in the reactant and product region.

State average orbitals were used in the excited-state MEP calculations:  $S_2, S_1$  state average orbitals (weights 0.50, 0.50) for the  $S_2$  MEPs, and  $S_1, S_0$  state average orbitals (weights 0.50, 0.50) for the  $S_1$  MEPs. The nature of the minima and transition states was confirmed by analytical or numerical (depending on the size of the active space) second derivative calculations and IRC method (in the case of transition states). The valence bond structures are obtained from a localized orbital analysis of the CASSCF wavefunction. The localized orbitals are generated using the Boys method<sup>27</sup> available in Gaussian.

At the computed critical points, CASPT2 energy calculations were carried out to include the necessary dynamic correlation effects by using the Molcas-5<sup>28</sup> program. The CASPT2/CASSCF protocol has proved this accuracy repeatedly.<sup>29–31</sup> Determination of the  $NEA^* \rightarrow S_1/S_0$  CI barrier has been carried out by performing CASPT2 calculations at selected points along the computed  $S_1$  CASSCF MEP (Figure S4 in the Supporting Information). The zeroth-order wave function used in the excited-state CASPT2 calculations was a four-root ( $S_0, S_1, S_2, S_3$ ) state average 14e/10o CASSCF wavefunction. (The energy difference between the  $S_2/S_1$  CI and  $S_1/S_0$  CI was obtained by comparing the energy of the  ${}^1\pi\pi^*$  state at the two crossings; the energy difference between the  $S_2/S_1$  CI and  $NEA^*$  by considering that of the  ${}^1n\pi^*$  state; the  $S_1$  barrier height was obtained as the energy difference between the highest and lowest  $S_1$  energy values along the  $NEA^* \rightarrow S_1/S_0$  CI coordinate.) Note that this wavefunction, while is the most appropriate to describe four states simultaneously since the orbitals are optimized as state average orbitals for the four states with equal weights, does not reproduce the degeneracy between the crossing states at the conical intersection points. Thus, for example, the energy gap at the  $S_2/S_1$  CI is 0.1 eV at the four-root state average CASSCF(14e/10o) level and is 0.01 eV at the two-root state average CASSCF(12e/9o) level ( $S_0, S_1, S_2$  weights = 0.00, 0.50, 0.50) employed to optimize the geometry. To compare the energies of ground-state structures, the zeroth-order wave function used in the ground-state CASPT2 calculation was a single-root ( $S_0$ ) 14e/10o CASSCF wavefunction.

Perturbation-modified CASSCF reference wavefunctions were used to compute transition dipole moments according to the CAS state interaction (CASSI) protocol.<sup>32</sup>

The  $S_0$  IPT coordinate of the model compound **1** and real pesticide **2** was studied at density functional theory (DFT) level by employing the B3LYP functional and the 6-31G\* basis set. Time-dependent (TD) DFT calculations were carried at the NEA derivative of **1** and **2** to compare the order and nature of the four lowest vertical electronic states for the two compounds by using the 6-31G\* and 6-311++G\*\* basis sets.

### 4. The Vertical Excited States of **1** and **2**

CASSCF and CASPT2 calculations on model **1** indicate the presence of three low-lying singlet excited states. With CASPT2,

- (22) Döpp, D. In *CRC Handbook of Organic Photochemistry and Photobiology*; Horspool, W. M., Song, P.-S., Eds.; CRC Press: Boca Raton, FL, 1995; p 1019.
- (23) Robb, M. A.; Garavelli, M.; Olivucci, M.; Bernardi, F. In *Reviews in Computational Chemistry*; Lipkowitz, K. B., Boyd, D. B., Eds.; Wiley-VCH: New York, Chichester, 2000; pp 87–146.
- (24) Blancafort, L.; Ogliaro, F.; Olivucci, M.; Robb, M. A.; Bearpark, M. J.; Sinicropi, A. Computational Investigation of Photochemical Reaction Mechanisms. In *Computational Methods in Photochemistry*, Kutateladze, A., Ed.; CRC Press: Boca Raton, 2005; pp 31–110.
- (25) Bearpark, M. J.; Robb, M. A.; Schlegel, H. B. *Chem. Phys. Lett.* **1994**, *223*, 269–274.
- (26) Frisch, M. J.; et al. *Gaussian 98*, Revision A.7; Gaussian Inc.: Pittsburgh PA, 1998.

- (27) Boys, S. F. *Rev. Mod. Phys.* **1960**, *32*, 296.
- (28) Andersson, K.; et al. *MOLCAS*, version 5.1; University of Lund, Sweden, 2000.
- (29) De Vico, L.; Garavelli, M.; Bernardi, F.; Olivucci, M. *J. Am. Chem. Soc.* **2005**, *127*, 2433–2442.
- (30) Gonzalez-Luque, R.; Garavelli, M.; Bernardi, F.; Merchan, M.; Robb, M. A.; Olivucci, M. *Proc. Natl. Acad. Sci. U.S.A.* **2000**, *97*, 9379–9384.
- (31) Migani, A.; Gentili, P. L.; Negri, F.; Olivucci, M.; Romani, A.; Favaro, G.; Becker, R. S. *J. Phys. Chem. A* **2005**, *109*, 8684–8692.
- (32) Malmqvist, P.-Å.; Roos, B. O. *Chem. Phys. Lett.* **1989**, *155*, 189–194.

**Table 2.** Ground and Excited CASPT2//CASSCF(14e/10o) Energies at the Optimized CASSCF(me/no) Geometries for Model 1.

geometry	state	active space	CASSCF (hartrees)	$\Delta E$ (kcal mol <sup>-1</sup> )	CASPT2 (hartrees)	$\Delta E$ (kcal mol <sup>-1</sup> [eV])	oscillator strength	charge separation
NEA	S <sub>0</sub>	(6e/5o) <sup>a</sup>	-336.60915 <sup>k</sup>	—	—	—	—	—
	S <sub>0</sub>	(14e/10o)	-336.631745 <sup>c</sup>	0.00 <sup>b</sup>	-337.52025	0.00 <sup>b</sup>	—	—
	S <sub>3</sub> <sup>1ππ*</sup>	(14e/10o)	-336.39354 <sup>d</sup>	142.67	-337.33654	115.20 [4.98]	0.21	0.67
	S <sub>2</sub> <sup>1nπ*</sup>	(14e/10o)	-336.44014 <sup>d</sup>	113.43	-337.35321	104.74 [4.45]	0.00	0.30
	S <sub>1</sub> <sup>1nπ*</sup>	(14e/10o)	-336.46355 <sup>d</sup>	98.74	-337.37311	92.26 [4.00]	0.00	0.28
	S <sub>0</sub>	(14e/10o)	-336.62090 <sup>d</sup>	0.00 <sup>b</sup>	-337.52013	0.00 [0.00] <sup>b</sup>	—	0.34
S <sub>2</sub> /S <sub>1</sub> CI	S <sub>2</sub> <sup>1ππ*</sup>	(12e/9o) <sup>a</sup>	-336.44956 <sup>e</sup>	—	—	—	—	—
	S <sub>1</sub> <sup>1nπ*</sup>	(12e/9o) <sup>a</sup>	-336.44930 <sup>e</sup>	—	—	—	—	—
	S <sub>3</sub> <sup>1nπ*</sup>	(14e/10o)	-336.411909 <sup>d</sup>	131.14	-337.34775	108.17	—	—
	S <sub>2</sub> <sup>1ππ*</sup>	(14e/10o)	-336.443882 <sup>d</sup>	111.08	-337.37564	90.66	—	—
	S <sub>1</sub> <sup>1nπ*</sup>	(14e/10o)	-336.447629 <sup>d</sup>	108.73	-337.38818	82.80	—	—
	S <sub>0</sub>	(14e/10o)	-336.553169 <sup>d</sup>	42.50	-337.48089	24.62	—	—
S <sub>1</sub> /S <sub>0</sub> CI	S <sub>1</sub> <sup>1ππ*</sup>	(10e/8o) <sup>a</sup>	-336.48021 <sup>f</sup>	—	—	—	—	—
	S <sub>0</sub>	(10e/8o) <sup>a</sup>	-336.48094 <sup>f</sup>	—	—	—	—	—
	S <sub>3</sub> <sup>1nπ*</sup>	(14e/10o)	-336.3630 <sup>d,h</sup>	161.81	-337.30113	137.42	—	—
	S <sub>2</sub> <sup>1nπ*</sup>	(14e/10o)	-336.37279 <sup>d,h</sup>	155.69	-337.25059	169.14	—	—
	S <sub>1</sub> <sup>1ππ*</sup>	(14e/10o)	-336.48006 <sup>d,h</sup>	88.38	-337.39461	78.76	—	—
	S <sub>0</sub>	(14e/10o)	-336.48720 <sup>d,h</sup>	83.90	-337.40549	71.93	—	—
NEA* <sup>i</sup>	S <sub>1</sub> <sup>1nπ*</sup>	(12e/9o) <sup>a</sup>	-336.50054 <sup>g</sup>	—	—	—	—	—
	S <sub>0</sub>	(12e/9o) <sup>a</sup>	-336.57958 <sup>g</sup>	—	—	—	—	—
	S <sub>3</sub> <sup>1nπ*</sup>	(14e/10o)	-336.41829 <sup>d</sup>	127.14	-337.36067	100.06	—	—
	S <sub>2</sub> <sup>1ππ*</sup>	(14e/10o)	-336.44422 <sup>d</sup>	110.87	-337.36573	96.88	—	—
	S <sub>1</sub> <sup>1nπ*</sup>	(14e/10o)	-336.49168 <sup>d</sup>	81.09	-337.40356	73.15	—	—
	S <sub>0</sub>	(14e/10o)	-336.57953 <sup>d</sup>	25.96	-337.49933	13.05	—	—
TS*	S <sub>1</sub> <sup>1nπ*</sup>	(12e/9o) <sup>a</sup>	-336.46883 <sup>j</sup>	—	—	—	—	—
	S <sub>3</sub> <sup>1nπ*</sup>	(14e/10o)	-336.38269 <sup>d</sup>	149.48	-337.32459	122.70	—	—
	S <sub>2</sub> ( <sup>1</sup> nπ* + <sup>1</sup> ππ*)	(14e/10o)	-336.40988 <sup>d</sup>	132.42	-337.34981	106.88	—	—
	S <sub>1</sub> ( <sup>1</sup> nπ* - <sup>1</sup> ππ*)	(14e/10o)	-336.45606 <sup>d</sup>	103.44	-337.38436	85.19	—	—
	S <sub>0</sub>	(14e/10o)	-336.53061 <sup>d</sup>	56.66	-337.46175	36.63	—	—
	S <sub>0</sub>	(6e/5o) <sup>a</sup>	-336.56404 <sup>k</sup>	—	—	—	—	—
TS	S <sub>0</sub>	(14e/10o)	-336.59828 <sup>c</sup>	21.00	-337.49365	16.69	—	—
	S <sub>0</sub>	(6e/5o) <sup>a</sup>	-336.58173 <sup>k</sup>	—	—	—	—	—
ANI	S <sub>0</sub>	(6e/5o) <sup>a</sup>	-336.58173 <sup>k</sup>	—	—	—	—	—
	S <sub>0</sub>	(14e/10o)	-336.60700 <sup>c</sup>	16.69	-337.49513	15.76	—	—

<sup>a</sup> For a description of the me/no active space see Computational Details. <sup>b</sup> Energies relative to the NEA S<sub>0</sub> energy. <sup>c</sup> One-root S<sub>0</sub> CASSCF(14e/10o) energy. <sup>d</sup> Four-root S<sub>3</sub>, S<sub>2</sub>, S<sub>1</sub>, and S<sub>0</sub> state average CASSCF(14e/10o) energy (weights = 0.25, 0.25, 0.25, 0.25). <sup>e</sup> Two-root S<sub>3</sub> and S<sub>2</sub> state average CASSCF(12e/9o) energy (weights = 0.50, 0.50). <sup>f</sup> Two-root S<sub>1</sub> and S<sub>0</sub> state average CASSCF(10e/8o) energy (weights = 0.50, 0.50). <sup>g</sup> Two-root S<sub>1</sub> and S<sub>0</sub> state average CASSCF(12e/9o) energy (weights = 0.50, 0.50). <sup>h</sup> S<sub>1</sub>/S<sub>0</sub> CI used for the CASPT2//CASSCF calculations corresponds to TS\* → ACI-like S<sub>1</sub>/S<sub>0</sub> CI MEP next-to-last point. <sup>i</sup> NEA\* corresponds to TS\* → NEA\* MEP last point. <sup>j</sup> One-root S<sub>1</sub> CASSCF(12e/9o) energy. <sup>k</sup> One-root S<sub>0</sub> CASSCF(6e/5o) energy.

the vertically excited S<sub>1</sub> and S<sub>2</sub> states are located at 4.0 and 4.5 eV, respectively, and have <sup>1</sup>nπ\* character with ca. zero oscillator strength, while the S<sub>3</sub> state appears at 5.0 eV with relatively high oscillator strength (Table 2).

The lower-energy <sup>1</sup>nπ\* state involves excitation from the n<sub>a</sub> orbital, whereas the higher-energy one involves excitation from the n<sub>s</sub> orbital. The S<sub>3</sub> state corresponds to a <sup>1</sup>ππ\* state. A Mulliken population analysis shows that it has a partial intramolecular charge separation character (from the enamine to the nitro group). If the molecule is divided into nitro and enamine fragments, these carry equal but opposite charges, with the negative charge on the electron-withdrawing nitro group. S<sub>0</sub> already features some degree of charge separation (*Q* = 0.34 au), but upon excitation to S<sub>3</sub> a moderate shift of electronic density ( $\Delta Q$  = 0.30 au) takes place from enamine to nitro fragments, leading to a higher degree of charge separation relative to S<sub>0</sub>.

Comparison between the model **1** and parent system **2** is made at the TDDFT level (Table 3). The TDDFT results for **1** are essentially co-incident with the CASPT2 data, predicting the same state ordering. For pesticide **2**, the S<sub>1</sub> state corresponds to <sup>1</sup>n<sub>a</sub>π\* as for model **1**, while the order between the S<sub>2</sub> and S<sub>3</sub> states is inverted, with S<sub>2</sub> corresponding to the <sup>1</sup>ππ\* state and S<sub>3</sub> to the <sup>1</sup>n<sub>s</sub>π\* state. TDDFT computation of the vertical excitation energies for **1** and **2** with the use of the larger

6-311++G\*\* basis set confirms the state ordering obtained at the lower TDDFT/6-31G\* level of theory. The only difference is that the vertical excitation energy to the <sup>1</sup>ππ\* state predicted by the larger basis set is lower with respect to the smaller basis set.

The TDDFT data with the larger 6311++G\*\* basis set for **2** agrees reasonably well with experiment.<sup>14</sup> As a reference value, we consider the experimental transition for **2** recorded in *n*-hexane (325 nm, 3.82 eV) which is 0.09, 0.38, and 0.72 eV below the S<sub>1</sub><sup>1</sup>n<sub>a</sub>π\*, S<sub>2</sub><sup>1</sup>ππ\*, and S<sub>3</sub><sup>1</sup>n<sub>s</sub>π\* states, respectively. However, the S<sub>0</sub>→S<sub>1</sub> and S<sub>0</sub>→S<sub>3</sub> transitions are calculated to be much weaker (*f* ≈ 0.00) than the S<sub>0</sub>→S<sub>2</sub> transition (*f* ≈ 0.42), suggesting that the S<sub>2</sub> state is the one pumped experimentally, as the experimental band is reported to be very intense ( $\epsilon$  = 40,000 at 365 nm in water).<sup>14</sup>

The path on the spectroscopic <sup>1</sup>ππ\* state, as discussed in the Introduction, has a steepest descent nature and after crossing the two <sup>1</sup>nπ\* states leads directly to the conical intersection with the ground state in model **1**. Consequently, in **1** both the <sup>1</sup>n<sub>a</sub>π\* and <sup>1</sup>n<sub>s</sub>π\* states might be partially populated through the conical intersections found along the <sup>1</sup>ππ\* MEP, that is a S<sub>3</sub>(<sup>1</sup>ππ\*)/S<sub>2</sub>(<sup>1</sup>n<sub>s</sub>π\*) CI and a S<sub>2</sub>(<sup>1</sup>ππ\*)/S<sub>1</sub>(<sup>1</sup>n<sub>a</sub>π\*) CI. On the other hand in **2**, the calculations predict only the existence of the S<sub>2</sub>(<sup>1</sup>ππ\*)/S<sub>1</sub>(<sup>1</sup>n<sub>a</sub>π\*) conical intersection since the <sup>1</sup>n<sub>s</sub>π\* state is computed above the <sup>1</sup>ππ\* state. Thus, in the following we avoid the

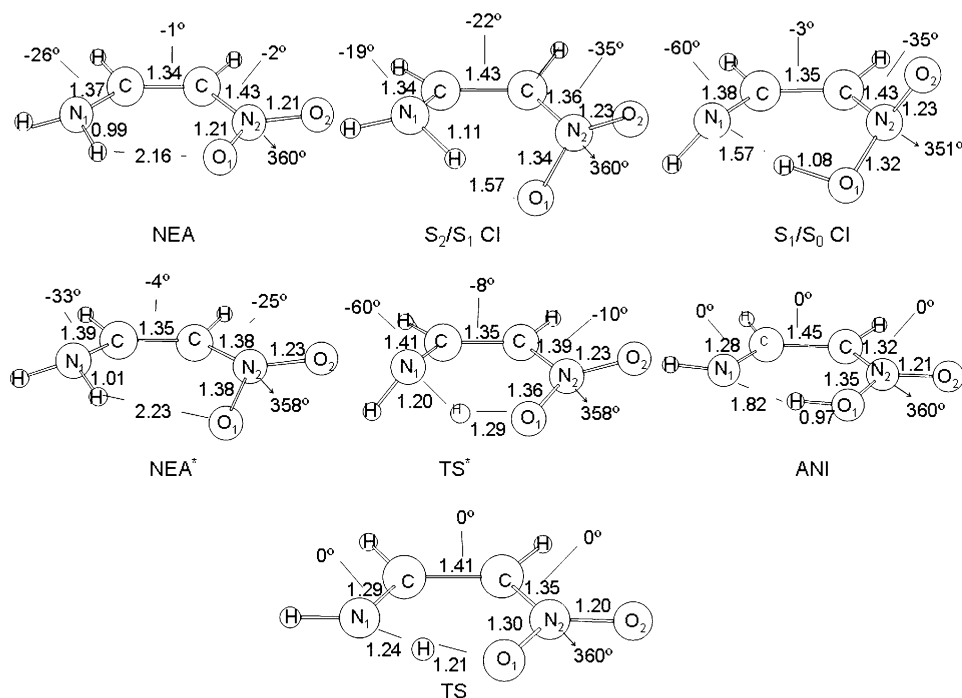


**Figure 2.** CASSCF/6-31G\* optimized geometries (relevant parameters in Å and deg) of the  $S_0$  nitro enamine minimum (NEA), the lowest energy  $S_2/S_1$  crossing point between  ${}^1\pi\pi^*$  and  ${}^1n\pi^*$  excited states ( $S_2/S_1$  CI), the lowest energy  $S_1/S_0$  crossing point between  ${}^1\pi\pi^*$  and ground states ( $S_1/S_0$  CI), the  $S_1$   ${}^1n\pi^*$  nitro enamine minimum (NEA\*), the  $S_1$  tautomerization transition state ( $TS^*$ ), the  $S_0$  acinitro imine minimum (ANI), and  $S_0$  tautomerization transition state (TS).

**Table 3.** DFT Energies for  $S_0$  Intramolecular Proton Transfer and TDDFT Excitation Energies for Model 1 and Pesticide 2 (Oscillator Strengths,  $f$ , in square brackets)

geometry	state	DFT 6-31G* (hartrees)	$\Delta E$ (kcal mol <sup>-1</sup> )	TDDFT 6-31G* (eV)	TDDFT 6-311++G** (eV)	experiment
Model System 1						
NVA	$S_0$	-338.46033	0.00 <sup>a</sup>	0.00 <sup>a</sup>	0.00 <sup>a</sup>	—
	$S_1$ ${}^1n\pi^*$			3.91 [0.00]	3.89 [0.00]	—
	$S_2$ ${}^1n\pi^*$			4.45 [0.00]	4.45 [0.00]	—
	$S_3$ ${}^1\pi\pi^*$			4.75 [0.24]	4.57 [0.26]	—
TS	$S_0$	338.43859	13.64			
ANI	$S_0$	-338.43903	13.37			
Real Pesticide 2						
NEA	$S_0$	-853.38321	0.00 <sup>a</sup>	0.00 <sup>a</sup>	0.00 <sup>a</sup>	—
	$S_1$ ${}^1n\pi^*$			3.91 [0.00]	3.91 [0.00]	—
	$S_2$ ${}^1\pi\pi^*$			4.36 [0.38]	4.20 [0.42]	365 nm (3.40 eV) <sup>b</sup>
	$S_3$ ${}^1n\pi^*$			4.52 [0.02]	4.54 [0.00]	325 nm (3.82 eV) <sup>c</sup>
TS	$S_0$	-853.36946	8.63			
ANI	$S_0$	-853.37014	8.20			

<sup>a</sup> Energies relative to the NEA  $S_0$  energy. <sup>b</sup> From ref 14: water. <sup>c</sup> From ref 14: *n*-hexane.

discussion of the  $S_3/S_2$  CI and of the relaxation paths starting at this intersection and consider only the  $S_2/S_1$  CI and corresponding relaxation paths which are predicted to be a common topological feature to **1** and **2**. (Discussion of the  $S_3/S_2$  CI and corresponding relaxation paths can be found in the Supporting Information. Hereafter the label *a* for antisymmetric and *s* for symmetric associated with the *n* orbitals is dropped, and the  ${}^1n_a\pi^*$  state is referred to as  ${}^1n\pi^*$ .)

### 5. The Phototautomerization Path Driven by the ${}^1\pi\pi^*$ State

The bold line in Figure 1 traces the evolution of the  ${}^1\pi\pi^*$  state. The geometries of the critical points encountered are shown in Figure 2, and their absolute and relative energies in Table 2.

The initial part of the reaction coordinate on the  ${}^1\pi\pi^*$  state leads to a rapid energy decrease, and results in the production of a transient NEA-like ‘spiral’ structure corresponding to an  $S_2/S_1$  conical intersection between the  ${}^1\pi\pi^*$  and  ${}^1n\pi^*$  excited states ( $S_2/S_1$  CI). At this ‘spiral’ structure, the distance between the hydrogen-bonded termini (i.e., H–O<sub>(1)</sub> distance) is substantially shortened (1.57 Å) with respect to that of the ground-state reactant (2.16 Å), and facile IPT can take place. We have ignored the crossing with the second  ${}^1n\pi^*$  state shown in Figure 1 for model **1**, as the  ${}^1\pi\pi^*$  state was already found to be  $S_2$  for pesticide **2** as described above.

We could locate two distinct pathways on the  $S_1$  surface originating at the  $S_2/S_1$  CI, identified by the IRD vectors reported in Figure 3. The pathway that remains on the  ${}^1\pi\pi^*$  electronic

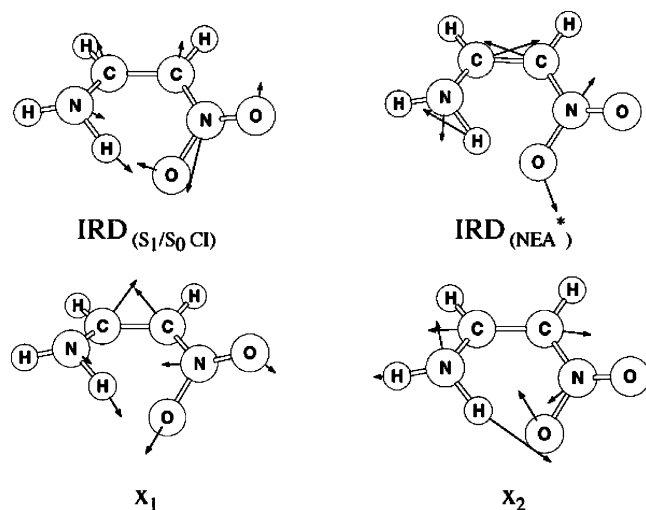


**Figure 3.** Initial relaxation directions that define the relaxation paths starting from the  $S_2/S_1$  CI on the  $S_1$  potential energy surface, toward the  $S_1/S_0$  CI ( $IRD_{(S_1/S_0\ CI)}$ ) and NEA\* minimum ( $IRD_{(NEA^*)}$ ). The gradient difference ( $x_1$ ) and derivative coupling ( $x_2$ ) directions that remove the degeneracy at  $S_2/S_1$  CI are also shown.

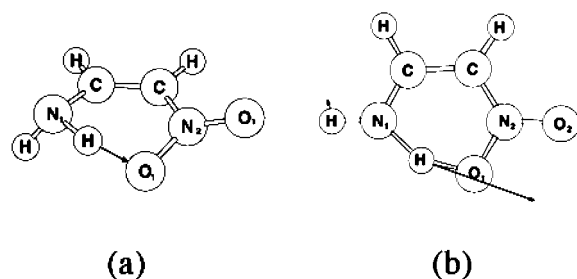


**Figure 4.** (a) Transition state vector associated with  $TS^*$ . (b) Transition state vector associated with  $TS$ .

state leads to an  $S_1/S_0$  conical intersection ( $S_1/S_0$  CI), which is located  $\sim 19$  kcal mol $^{-1}$  below the  $S_2/S_1$  CI. As shown by the  $IRD_{(S_1/S_0\ CI)}$  vector at the  $S_2/S_1$  CI, this pathway is dominated by out-of-plane motion (C–C torsion and  $NO_2$  pyramidalization) and  $N_{(1)}$ -H stretching. The resulting  $S_1/S_0$  CI geometry has an ANI-like structure ( $N_{(1)}$ -H = 1.57 Å and  $O_{(1)}$ -H = 1.08 Å) with the nitron group ( $NO_2H$ ) pyramidalized, and the central C–C double bond regenerated.

In contrast, the path from the  $S_2/S_1$  CI on the  ${}^1n\pi^*$  potential energy surface leads to an  ${}^1n\pi^*$  excited-state minimum (NEA\*) located  $\sim 10$  kcal mol $^{-1}$  below. This path is identified by the  $IRD_{(NEA^*)}$  vector, and has a large component of  $N_{(1)}$ -H and  $N_{(2)}$ - $O_{(1)}$  stretching and  $N_{(1)}CCN_{(2)}$  bond inversion. Consistently, at NEA\* the  $O_{(1)}$ -H distance is large (2.23 Å), and the single/double/single bond skeletal pattern is restored. Note also that the  $N_{(2)}$ - $O_{(1)}$  bond is stretched (1.38 Å), in line with the fact that this structure correlates with the  ${}^1n\pi^*$  excited state at the FC region.

The NEA\* minimum is separated from the ANI-like  $S_1/S_0$  CI by a sizable activation barrier (ca. 12 kcal mol $^{-1}$ ) on  $S_1$ , due to an avoided crossing with the  ${}^1\pi\pi^*$  state represented by  $TS^*$  ( $-1872.8$  cm $^{-1}$  imaginary frequency). At  $TS^*$ , the hydrogen is half the way between the nitrogen and oxygen atoms ( $N_{(1)}$ -H = 1.20 Å, H- $O_{(1)}$  = 1.29 Å). This structure features a quasi-planar disposition of the six cycle members, and the transition state vector (Figure 4a) describes the in-plane migration of H. Because of the barrier from NEA\* to the ANI-like

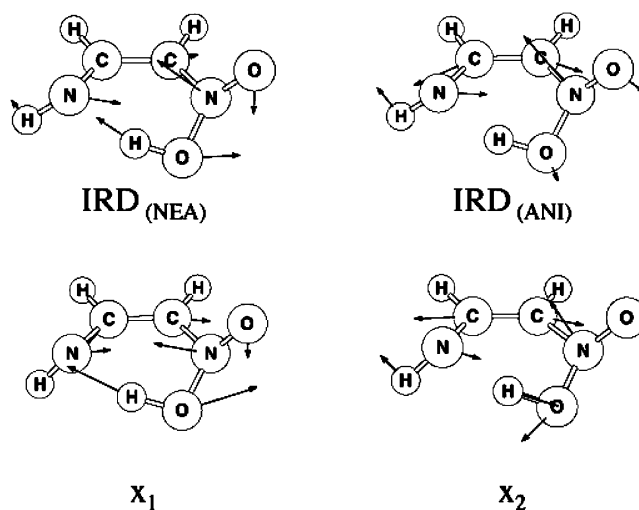


**Figure 5.** Initial relaxation directions that define the relaxation paths starting from  $S_1/S_0$  CI on the  $S_0$  potential energy surface toward the ANI ( $IRD_{(ANI)}$ ) and NEA ( $IRD_{(NEA)}$ ) tautomers. The gradient difference ( $x_1$ ) and derivative coupling ( $x_2$ ) directions that remove the degeneracy at the  $S_1/S_0$  CI are also shown.

region of  $S_1$ , other reactions of NEA\* are likely to occur, leading to photodegradation, as will be described in more detail in the next section (and in a subsequent paper).

From the  $S_1/S_0$  CI, two different relaxation pathways could also be located, identified by the IRD vectors shown in Figure 5. The IRD vector that defines the relaxation back toward the ground-state NEA tautomer ( $IRD_{(NEA)}$ ) is dominated by the proton-transfer coordinate, while the IRD pointing toward the ANI tautomer ( $IRD_{(ANI)}$ ) by skeletal stretching. Both vectors have an  $NO_2H$  out-of-plane mode component. Once formed, ANI returns to the more stable NEA through a thermal pathway on the ground state, via the transition state structure  $TS$  ( $-2011.4$  cm $^{-1}$  imaginary frequency at the CASSCF level and  $-750.3$  cm $^{-1}$  at the DFT level). (This path is not shown in Figure 1, as it is characterized by a planar reaction coordinate, Figure 4b, which is quite different to the others already shown.) The barrier associated with  $TS$  amounts to  $\sim 1$  kcal mol $^{-1}$  for the ANI→NEA direction, and  $\sim 17$  kcal mol $^{-1}$  for the NEA→ANI direction at the CASPT2//CASSCF level. The barriers estimated by DFT calculations (Table 3) are  $\sim 14$  and  $\sim 1$  kcal mol $^{-1}$  for the forward and reverse proton transfer, respectively, in agreement with the CASPT2//CASSCF data. Accordingly, once formed the ANI tautomer efficiently reverts to the NEA starting form through an essentially barrierless pathway. For pesticide **2**, the DFT calculations predict a barrierless path ( $< 1$  kcal mol $^{-1}$ ) for back-proton transfer on  $S_0$ , and a barrier height of  $\sim 8$  kcal mol $^{-1}$  separating the NEA from the ANI tautomer and a  $-950.2$  cm $^{-1}$  imaginary frequency.

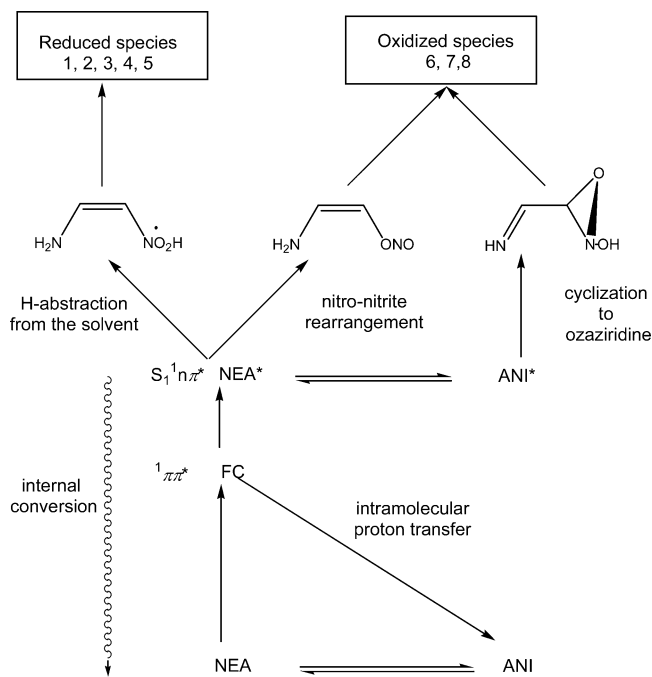
Throughout the decay of the  ${}^1\pi\pi^*$  state (Figure 1), the reaction coordinate is contained in the branching plane, defined by the directions that remove the degeneracy at the  $S_2/S_1$  and  $S_1/S_0$  conical intersections. Let us compare the gradient difference and derivative coupling vectors shown in Figures 3 and 5, with the corresponding IRDs shown in the same figures. As an example, the gradient difference and derivative coupling vectors at  $S_2/S_1$  CI both have a large skeletal stretching at the C–C bond, which is in agreement with the fact that all structures optimized on the  $S_1$  surface,  $TS^*$ , NEA\*, and  $S_1/S_0$  CI, and the FC structure (NEA) have the central C–C bond fully regener-



ated, whereas at the  $S_2/S_1$  crossing the C–C bond corresponds to a single bond. The gradient difference also has a large component of  $\text{NO}_2$  torsion, which is in agreement with the fact that torsion about the C– $\text{N}_{(2)}$  bond is important both on the  $S_2$  (compare FC to  $S_2/S_1$  CI) and  $S_1$  (compare  $S_2/S_1$  CI to  $\text{TS}^*$  and  $\text{NEA}^*$ ) reaction coordinates. It can be seen that the gradient difference and the  $\text{IRD}_{(S_1/S_0 \text{ CI})}$  vector have similar  $\text{N}_{(1)}\text{–H}$  stretching components. Moreover, the derivative coupling vector is essentially the  $\text{IRD}_{(\text{NEA}^*)}$  vector with opposite sign. Note that the transition vector for  $\text{TS}^*$  ( $\text{N}_{(1)}\text{–H}$  stretching) also lies in the branching space. An analogous situation occurs for the  $S_1/S_0$  CI. The gradient difference vector is essentially the  $\text{IRD}_{(\text{NEA})}$  vector. The derivative coupling vector also shows some overlap with the  $\text{IRD}_{(\text{ANI})}$  vector with respect to the  $\text{N}_{(1)}\text{–H}$  torsion and  $\text{N}_{(1)}\text{CCN}_{(2)}$  skeletal stretching. Consequently, the  $S_2/S_1$  and  $S_1/S_0$  conical intersections are directly accessible, and rapid radiationless decay can take place. Although ANI can be formed photochemically from NEA, the reactants are recovered thermally, leading to overall photostability provided that leakage to  $\text{NEA}^*$  has not taken place. We discuss the consequences of this excited-state leakage in the next section.

The ESIPT mechanism documented for **1** agrees with the mechanism derived for related compounds, salicylic acid,<sup>33,34</sup> *o*-hydroxybenzaldehyde,<sup>35</sup> 7-hydroxy-1-indanone,<sup>35</sup> malonaldehyde,<sup>9</sup> and 2-(2'-hydroxyphenyl)benzotriazole<sup>36</sup> between them. These studies which employ electron-correlated methods (CASPT2, TDDFT, or more recently CC2) predict a significant barrier on the  $S_1$   $^1n\pi^*$  state<sup>9</sup> and a barrierless profile for the  $^1\pi\pi^*$  state-driven intramolecular proton- or hydrogen-transfer process. For efficient  $S_1$  to  $S_0$  radiationless decay, different types of conical intersections have been proposed. A dissociative  $^1\pi\sigma^*$  state has been identified for malonaldehyde,<sup>9,35,37</sup> and various intramolecular hydrogen-bonded aromatic systems,<sup>35</sup> leading to a conical intersection with the ground state along a hydrogen-detaching coordinate. The  $^1\pi\pi^*$  state is separated from the  $S_1$ -( $^1\pi\sigma^*$ )/ $S_0$  CI via a small energy barrier due to the avoided crossing between the  $^1\pi\pi^*$  and  $^1\pi\sigma^*$  states. A conical intersection between the  $^1n\pi^*$  state and the ground state has been found for (2-(2'-hydroxyphenyl)triazole)<sup>3</sup> and a truncated subsystem<sup>6</sup> which is accessed in the parent compound after  $^1\pi\pi^* \rightarrow ^1n\pi^*$  state switch along the proton-transfer coordinate. In *o*-(hydroxyphenyl)-(1,3,5)triazine<sup>38</sup> radiationless decay to the ground state is associated with an extended seam of  $S_1/S_0$  intersection lying parallel to the ESIPT path with sloped<sup>39</sup> topology which can be accessed at any point along the reaction path by nuclear motion orthogonal to the reaction coordinate involving only the skeletal stretching and no motion of the hydrogen. Very recently, two studies on salicylic acid<sup>34</sup> and 2-(2'-hydroxyphenyl)benzotriazole<sup>36</sup> have shown that a conical intersection with the ground state can be accessed without a barrier from the  $^1\pi\pi^*$  along a combination of twisting and pyramidalization coordinates, thus providing further evidence for the importance of the

Scheme 2



interplay between the proton (hydrogen) transfer and twisting and pyramidalization modes in ESIPT. Contrary to NEA, in these studies it is seen that the hydrogen transfer, and twisting and pyramidalization modes are decoupled, and the conical intersection with the ground state is attained at a keto-like twisted configuration with very weak intramolecular hydrogen bonding. Despite these differences, it seems that the conical intersection responsible for ultrafast deactivation to  $S_0$  in NEA is of the same type as that reported for salicylic acid and 2-(2'-hydroxyphenyl)benzotriazole, the three of them corresponding to dot–dot/hole-pair twisted structures. Thus, this study provides further evidence for the importance of this type of conical intersection in ESIPT.

## 6. The Photodegradation Mechanism Based on the $S_2/S_1$ Intersection.

Because the barrier associated with  $\text{TS}^*$  cannot be easily overcome, the system will follow alternative nonreversible photochemical routes from  $\text{NEA}^*$  typical of the nitro group  $^1n\pi^*$  state<sup>22</sup> leading to the degradation of the molecule, or internal conversion paths. These paths are summarized in Scheme 2 and will be discussed more extensively in a separate paper; what follows is an overview.

In Scheme 2 the primary photochemical events identified for **1** are related to the photodegradation products observed experimentally for **2** and reported in Table 1. As discussed below, the model calculations reported can be used to interpret the behavior of **2** in low-polarity solvents (i.e., dichloromethane). These can be classified in terms of two structural types: (i) reduced species (such as 1, 2, 3, 4, 5) where the nitro moiety is reduced and (ii) oxidized species (such as 6, 7, and 8) where the nitro group is oxidized. Note that the degradation does not involve the heterocyclic ring, and therefore the model **1** is suitable to study the deactivation of the  $S_1$   $^1n\pi^*$  state. Scheme 2 shows that three photochemical and one unreactive internal

(33) Sobolewski, A. J.; Domcke, W. *Chem. Phys.* **1998**, *232*, 257–265.

(34) Sobolewski, A. J.; Domcke, W. *Phys. Chem. Chem. Phys.* **2006**, *8*, 3410–3417.

(35) Sobolewski, A. J.; Domcke, W. *Phys. Chem. Chem. Phys.* **1999**, *1*, 3065–3072.

(36) Sobolewski, A. L.; Domcke, W.; and Hattig, C. *J. Phys. Chem. A* **2006**, *110*, 6301–6306.

(37) Sobolewski, A. J.; Domcke, W. *Chem. Phys. Lett.* **1999**, *300*, 533–539.

(38) Paterson, M. J.; Robb, M. A.; Blancafort, L.; DeBellis, A. D. *J. Phys. Chem. A* **2005**, *109*, 7527–7537.

(39) Atchity, G. J.; Xantheas, S. S.; Ruedenberg, K. *J. Chem. Phys.* **1991**, *95*, 1862.

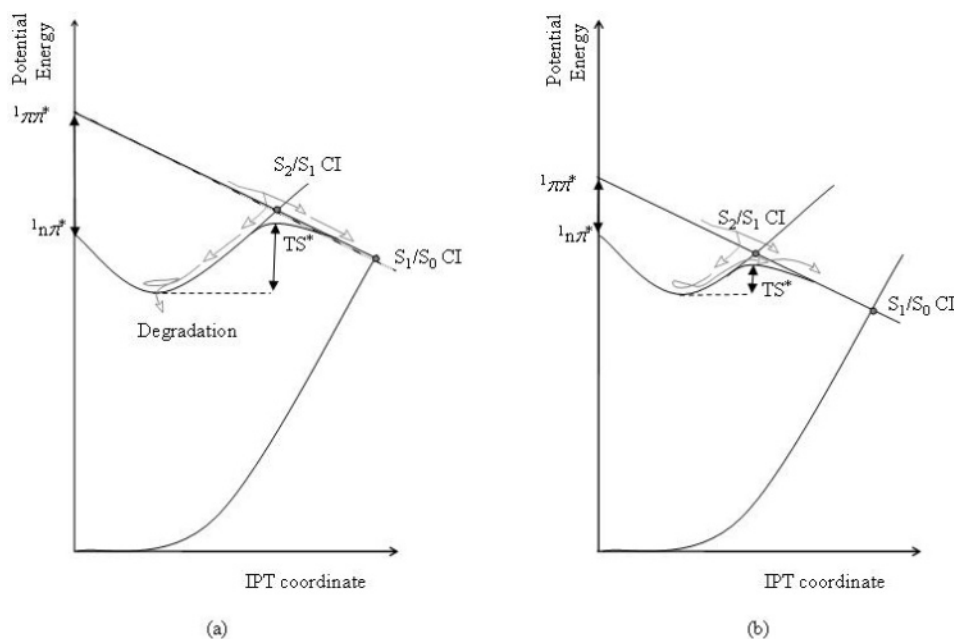


**Figure 6.** Effect of the variation in energy of the  $^1\pi\pi^*$  state relative to the  $^1n\pi^*$  state at the FC point on the  $S_1$  barrier. (a) Large separation  $\rightarrow$  sizable barrier. (b) Small separation  $\rightarrow$  small barrier.

conversion path have been located connecting  $S_1$  to  $S_0$ .<sup>40</sup> All these decay routes are found to occur nonadiabatically, via a  $S_1/S_0$  conical intersection located at some point along the reaction coordinate.

Radiationless decay on the NEA\* side occurs along a H-abstraction from the solvent coordinate<sup>22</sup> leading to the formation of the reduced species. The nitrile derivative (species 3) is not usually reported as a secondary product of the H-abstraction from the solvent, but it may be generated by loss of one water molecule from species 2 (Table 1). NEA\* may also deactivate through a nitro nitrite rearrangement<sup>22</sup> coordinate. There is an additional reactive coordinate which involves an adiabatic IPT on the  $S_1$  state prior to radiationless decay along a nonadiabatic cyclization to oxaziridine<sup>41</sup> coordinate. This IPT path does not correspond to the NEA\* $\rightarrow$  $S_1/S_0$  CI or the  $S_2/S_1$  CI $\rightarrow$  $S_1/S_0$  CI IPT paths reported in Figure 1, but lies in the “moat” surrounding the  $S_1/S_0$  CI on the  $S_1$  surface, and leads to an  $S_1$  excited-state intermediate of the ANI tautomer, ANI\* (not shown in Figure 1). The formation of ANI\* is irreversible as the cyclization to oxaziridine route has a lower activation barrier compared to that for back IPT to regenerate NEA\*. The nitro nitrite rearrangement and cyclization to oxaziridine are similar in the sense that they both correspond to a cyclization coordinate in which a  $\sigma$  bond is formed between the nitro/nitron group oxygen and the  $\alpha$ -carbon atom, and they can in principle both be responsible for the formation of the oxidized species. Radiationless decay through the internal conversion path leads to the regeneration of the reactant.

The existence of nonradiative decay channels has also been reported for the photodissociation of nitromethane<sup>42–44</sup> and the

nitramide,<sup>45</sup> and for the  $\text{NO}_2$   $\sigma$  radical.<sup>46–48</sup> However, no degradation products originating from the C–N bond scission are evident in the photolysate of pesticide **2**, suggesting that these mechanisms are not operative.

The central issue to understand the photostability is the relative ordering and steepness of the  $^1\pi\pi^*$  and  $^1n\pi^*$  states and their coupling. In vacuo, where the  $^1n\pi^*$  state lies below the  $^1\pi\pi^*$  state, the photodegradation depends on the branching ratio at the  $S_2/S_1$  CI, which in turn is influenced by the relative steepness of the  $^1n\pi^*$  and the  $^1\pi\pi^*$  surfaces and their electronic coupling. For model **1** and presumably for pesticide **2**, the  $^1\pi\pi^*$  surface is less steep than the  $^1n\pi^*$  surface (Figures 1 and S1), and the two states are coupled as indicated by the derivative coupling vector length. In this case there is some probability to decay to the  $^1n\pi^*$  surface, and the photodegradation depends on the competition between the NEA\* $\rightarrow$  $S_0/S_1$  CI route through TS\* and the other decay pathways available to the NEA\* intermediate (shown in Scheme 2). Stabilization of the  $^1\pi\pi^*$  state as shown in Figure 6 by appropriate substituents, such as in structure **3** (Scheme 1) bearing an electron-donating group (EDG) in conjugation with the chromophore, or by polar solvents should improve the photostability by lowering the barrier to access the  $S_0/S_1$  CI from NEA\*, and the ideal situation for photostability would be achieved by reversing the order of the  $^1\pi\pi^*$  and  $^1n\pi^*$  states.

The present stability model, formulated on the basis of calculations in vacuo, can explain the experimental results<sup>14</sup> in dichloromethane satisfactorily. First of all, the DFT calculations for **2** predict that the back-proton-transfer process on  $S_0$  is essentially barrierless. The calculations do not include the effect

(40) Migani, A. Ph.D., University of London, London, 2001.  
 (41) Albini, A.; Fasani, E.; Amer, A. In *CRC Handbook of Organic Photochemistry and Photobiology*, Horspool, W. M., Song, P.-S., Eds.; CRC Press: Boca Raton, FL, 1995; p 879.  
 (42) Arenas, J. F.; Otero, J. C.; Peláez, D.; Soto, J. *J. Chem. Phys.* **2003**, *119*, 7814–7823.  
 (43) Arenas, J. F.; Otero, J. C.; Peláez, D.; Soto, J. *J. Chem. Phys.* **2005**, *122*, 084324.  
 (44) Roszak, S.; Kaufman, J. *J. Chem. Phys.* **1991**, *94*, 6030–6035.

(45) Arenas, J. F.; Otero, J. C.; Peláez, D.; Soto, J. *J. Phys. Chem. A* **2005**, *109*, 7172–7180.  
 (46) Blahous, C. P., III; Yates, B. F.; Xie, Y.; Schaefer, H. F., III. *J. Chem. Phys.* **1990**, *93*, 8105–8109.  
 (47) Kurkal, V.; Fleurat-Lessard, P.; Schinke, R. *J. Chem. Phys.* **2003**, *119*, 1489–1501.  
 (48) Leonardi, E.; Petrongolo, C.; Hirsh, G.; Buenker, R. *J. Chem. Phys.* **1996**, *105*, 9051–9067.

of the solvent on the reaction barriers, but it is plausible that the barrier heights will not change in low-polarity solvents (e.g., dichloromethane). Accordingly, in dichloromethane the degradation is not due to ground-state reactivity of the ANI derivative. Moreover, the TDDFT calculations for **2** support the existence of the  $S_1/S_2$  CI in vacuo since the  ${}^1\pi\pi^*$  state is computed above one  ${}^1n\pi^*$  state. In dichloromethane, due to the low solvent polarity, the order of the states will most probably coincide with that computed for **2** in vacuo. In fact the main degradation product in  $\text{CH}_2\text{Cl}_2$  is the nitrile derivative (species 3),<sup>14</sup> which is interpreted as a secondary product of H-abstraction from the solvent<sup>22</sup> carried out by the  ${}^1n\pi^*$  state minimum NEA\*. Clearly, the  $S_2/S_1$  CI geometry and topography might be slightly different from those computed for **1**, but the large coupling between the two states should be preserved, implying that there is some probability to change electronic state upon decay at the  $S_2/S_1$  CI also for pesticide **2**. A quantitative measure of the probability of decaying on the  ${}^1n\pi^*$  state at  $S_2/S_1$  CI and partitioning between the competing  ${}^1n\pi^*$  pathways can only be obtained through a dynamical treatment including the solvent and the heterocyclic ring in the calculations.

In water or methanol, the photodegradation is substantially slower than in dichloromethane,<sup>13,14</sup> which agrees with our proposal that stabilization of the  ${}^1\pi\pi^*$  state will increase the stability. The involvement of the  ${}^1n\pi^*$  state in water and methanol is suggested by the fact that the main photoproduct is a possible secondary product after H-abstraction from the solvent<sup>22</sup> by the  ${}^1n\pi^*$  state minimum, although a different one from the main product in dichloromethane. However, we cannot exclude the alternative situation where, due to the high polarity of the solvents and their hydrogen-bonding ability, the order of the states may be reversed. This would make population of the  ${}^1n\pi^*$  state through an  $S_1/S_2$  CI unlikely, and the photodegradation would have to occur via a different mechanism. Nevertheless, the main features of the tautomerization mechanism and the associated  $S_1/S_0$  conical intersection are probably still valid in water, as the experimental results indicate that phototautomerization is the fastest process in that solvent.<sup>14</sup> In any case, the study of the photoreactivity in water would require a complex computational treatment in the line with recent work on the photophysics of uracil derivatives<sup>49–51</sup> in water, but these calculations are out of the scope of this paper.

## 7. Conclusions

A delicate balance between photostability and photodegradation has been identified in the NEA class of pesticides. The phototautomerization coordinate has been studied using CASS-

CF model calculations. This reaction pathway is ultimately unreactive (because of a thermal back-reaction), contributing to the photostability of NEA.

The phototautomerization mechanism described in this paper has two important features: optical absorption to a  ${}^1\pi\pi^*$  state with a charge separation character, and diabatic correlation between the resulting FC charge-separated structure and the tautomerized form on the ground state. This simple correlation suggests that the proton transfer takes place entirely on the  ${}^1\pi\pi^*$  diabatic surface, and will proceed without a barrier. The efficiency of this mechanism depends on whether the  ${}^1\pi\pi^*$  state corresponds to the lowest excited state  $S_1$  or not. If the  ${}^1\pi\pi^*$  state corresponded to  $S_1$ , efficient formation of the ANI tautomer would take place upon decay at a low-lying  $S_1/S_0$  conical intersection. With this condition satisfied, the phototautomerization coordinate could be used as a reliable photostabilization mechanism (i.e., benign dissipation of light energy as heat) provided that the tautomerized form could easily revert on the ground state to the starting tautomer via a facile thermal reaction.

However, phototautomerization in the NEAs studied here only partially conforms to the mechanism described above, because the  ${}^1\pi\pi^*$  state does not correspond to  $S_1$  but to a higher excited state. The lowest-lying states in these NEAs are  ${}^1n\pi^*$  excited states, and additional surface crossings between these and the  ${}^1\pi\pi^*$  state will be encountered before reaching the low-lying  $S_1/S_0$  conical intersection. These additional crossings provide a mechanism of population of the  ${}^1n\pi^*$  manifold, and subsequent photodegradation. The above results indicate that the high photolability observed for the pesticide<sup>14</sup> can be ascribed to photochemistry originating on the  ${}^1n\pi^*$  manifold of states, populated indirectly from the  ${}^1\pi\pi^*$  state. Prevention of this degradation could be engineered by ensuring that the first excited-state corresponds to the  ${}^1\pi\pi^*$ .

**Acknowledgment.** All computations were carried out on an IBM-SP2 funded jointly by IBM-UK and HECCE (UK). Dupont Central Research (Delaware) provided financial support for this project to A.M., M.J.B., and M.A.R. A.M. acknowledges support by the European Community through a Marie Curie fellowship (MEIF-CT-2003-500155). M.O. is grateful for the funding provided by the Università di Siena (progetto di Ateneo A. A. 02/04) and the HFSP (RG 0299/2000-M).

**Supporting Information Available:** Computed minimum energy path coordinates (Figures S1, S2, S3), discussion on the validation of the computational strategy and relaxation on the  ${}^1n_s\pi^*$  state (Table S1, Figures S4, S5), complete refs 26 and 28, and tables of Cartesian coordinates (XYZ) for the CASSCF/ and DFT/6-31G\* optimized structures. This material is available free of charge via the Internet at <http://pubs.acs.org>.

JA066592O

(49) Gustavsson, T.; Banyasz, A.; Lazzarotto, E.; Markovitsi, D.; Scalmani, G.; Frish, M. J.; Barone, V.; Impronta, R. *J. Am. Chem. Soc.* **2005**, *128*, 607–619.

(50) Gustavsson, T.; Sarkar, N.; Lazzarotto, E.; Markovitsi, D.; Barone, V.; Impronta, R. *J. Phys. Chem. B* **2006**, *110*, 12843–12847.

(51) Impronta, R.; Barone, V. *J. Am. Chem. Soc.* **2004**, *126*, 14320–14321.